

Effect of Laser Power and Scan Speed on Melt Pool Characteristics of Commercially Pure Titanium (CP-Ti)

Chandrakanth Kusuma, Sazzad H. Ahmed, Ahsan Mian, and Raghavan Srinivasan

(Submitted November 9, 2016; in revised form February 24, 2017; published online June 12, 2017)

Selective laser melting (SLM) is an additive manufacturing technique that creates complex parts by selectively melting metal powder layer-by-layer using a laser. In SLM, the process parameters decide the quality of the fabricated component. In this study, single beads of commercially pure titanium (CP-Ti) were melted on a substrate of the same material using an in-house built SLM machine. Multiple combinations of laser power and scan speed were used for single bead fabrication, while the laser beam diameter and powder layer thickness were kept constant. This experimental study investigated the influence of laser power, scan speed, and laser energy density on the melt pool formation, surface morphology, geometry (width and height), and hardness of solidified beads. In addition, the observed unfavorable effect such as inconsistency in melt pool width formation is discussed. The results show that the quality, geometry, and hardness of solidified melt pool are significantly affected by laser power, scanning speed, and laser energy density.

Keywords melt pool, process parameters, selective laser melting

1. Introduction

Selective laser melting (SLM) (Ref 1-4) is an additive manufacturing (AM) technology where a laser is used to selectively melt and fuse successive powder layers to build a component. The process involves rapid melting and solidification after a laser strikes a region of powder. A number of parameters influence the quality of parts fabricated by SLM process. Laser surface modification (LSM) also involves the use of laser to remelt material surfaces to modify surface mechanical properties. The mechanical properties that are shown to improve are corrosion, wear resistance, and also fatigue properties (Ref 5-7). By appropriate analysis of process parameters, the various factors that play a role in designing both the SLM and LSM processes can be explored. Stwora and Skrabalak (Ref 1) determined the influence of parameters such as laser power, point distance, scanning speed, and exposure time on tool steel components fabricated by selective laser sintering process. Yap et al. (Ref 2) reviewed research articles on SLM materials and their applications and discussed various properties such as microhardness, strength, and surface roughness of parts manufactured by SLM. Aboulkhair et al. (Ref 3) generated a list of controlling process parameters for SLM processing of AlSi10 Mg including (a) laser-related: laser source, laser power, and laser beam diameter/spot size; (b) scan-related: scan speed, scanning pattern, and scan spacing/hatch space; (c) powder-related: powder shape, powder size, particle distribution, powder morphology, powder density, and

layer thickness; and (d) temperature-related: powder bed temperature, powder feeder temperature, and temperature uniformity. Kurzynowski et al. (Ref 4) investigated effects of process parameters such as laser power, layer thickness, and the distance between scanning lines on the density of produced steel 316L (AISI), tool steel H13 (AISI), and titanium alloy Ti6Al7Nb (ISO 5832-11) products.

Selection of laser power is related to the size of the focused laser spot and determines the choice of other parameters of the process. The quality and the properties of SLM parts need fine tuning of parameters to optimize the energy density involved in the process. The laser energy density is a measure of the average applied energy per volume of the material during the scanning of a layer and quantifies energy input and is a key factor that affects the quality of the build component. In order to assess the combined effect of laser power (P) and scan speed (v) on individual line scanning, an integrated parameter called “linear laser energy density” (LED) is defined as follows to estimate the laser energy input to the powder layer being melted (Ref 8).

$$\text{Liner Energy Density, LED} = \frac{P}{v} \text{ J/mm} \quad (\text{Eq 1})$$

In Eq 1, P is laser power (W) and v is laser scan speed (mm/s). The overall effect of increasing power is to allow melting at faster speeds and greater depths of heat penetration. The faster the scan speed, the less time is available for heating and therefore, for a given laser power, less time for the heat to diffuse sideways, causing a narrowing of the melt region and heat-affected zone.

Titanium has a major application in biomedical especially for implants and load-bearing applications. Barbas et al. (Ref 9) used CP-Ti to develop porous structure as a bone substitute by SLM. Lipinski et al. (Ref 10) determined fatigue behavior of samples processed by SLM of CP-Ti grade 2. Hence, it is important to perform research on the melt pool characteristics of sintered CP-Ti. Attar et al. (Ref 11) studied the manufacturing of commercially pure titanium (CP-Ti) parts using SLM and powder with a particle size of 100 μm . An optimum set of

Chandrakanth Kusuma, Sazzad H. Ahmed, Ahsan Mian and Raghavan Srinivasan, Department of Mechanical and Materials Engineering, Wright State University, Dayton, OH 45458. Contact e-mail: ahsan.mian@wright.edu.

SLM process parameters was applied resulting in near full density (99.5%) without any post-treatments. They also conducted compressive strength, tensile strength and microhardness measurements of SLM-processed CP-Ti parts and compared the results with the properties of those manufactured by conventional/traditional manufacturing technologies. They found that the optimum manufacturing parameters improved the hardness and strength of SLM CP-Ti while maintaining the ductility. Tolosa et al. (Ref 12) performed similar studies, using 316 stainless steel powder. They manufactured tensile test specimen with different manufacturing strategies and compared their properties with wrought products. They used a layer thickness of 30 and 100 μm , scan speed up to 1000 mm/s and a laser spot size of 80-300 μm . They found that the strength of SLM material was higher than corresponding properties in the rolled condition. Charpy test results showed slightly lower toughness than those specified for wrought products. Hardness tests (Vicker's) results were homogeneous and similar to those found in wrought products of this alloy. Zhang et al. (Ref 8) published a review paper on the recent progress in SLM of Ti alloys and Ti composites for biomedical applications, especially in developing a new titanium powder for SLM. They discussed the parameters involved in SLM technology and included information about conditions that lead to undesirable phenomena such as balling in the melt pool. They also discussed the relationship between SLM processing parameters and final properties and microstructure of the different Ti alloys. SLM of CP-Ti was also investigated by other researchers (Ref 13-15) where the physical-mechanical properties such as surface roughness, wear performance, hardness and strength of test structures were evaluated. However, the study on the influence of process parameters on solidified melt pool geometry such as melt pool width and height for CP-Ti material is very limited.

In this study, the effect of laser power and scan speed on melt pool geometry and hardness of solidified melt pool was studied by conducting single bead experiments with commercially pure titanium (CP-Ti) using an in-house built SLM machine. The results obtained from this study would be beneficial in understanding the influence of laser parameters on solidified melt pools generated in powder bed SLM and LSM processes. The specific technical objectives of this study are summarized as below:

- Analyze the surface morphology of single beads/melt pools produced by SLM using multiple combinations of laser power and scan speed.
- Analyze the unfavorable effects such as inconsistent melt pool width formation.
- Measure the melt pool geometry (width and height) and investigate the effect of laser power and scan speed, laser energy density on melt pool geometry.
- Study the effect of laser power and scan speed, and laser energy density on mechanical properties such as hardness.
- Suggest the optimal parameters in the perspective of better mechanical properties such as hardness.

2. Materials and Sample Preparation

SLM single bead experiments were conducted to analyze the effect of laser power, scan speed, and laser energy density on

Table 1 Chemical composition of CP-Ti

Element	wt. %
Carbon	0.02
Oxygen	0.18-0.25
Nitrogen	0.02
Hydrogen	0.01
Iron	0.05-0.20
Titanium	Balance

Table 2 Parameters used to prepare the powder case sample

Parameter	Level
Laser power, P , W	100, 120, 140, 160, 180
Scan speed, v , mm/s	150, 200, 300, 500, 600
Laser beam diameter, d , μm	100
Layer thickness, t , μm	50

Table 3 Parameters used to prepare no-powder case sample

Parameter	Level
Laser power, P , W	276, 318, 360
Scan speed, v , mm/s	20, 60, 100
Laser beam diameter, d , μm	115

melt pool geometry and hardness of solidified melted zone using CP-Ti in both bulk (for substrate) and powder (for producing beads) forms. The powder particles were mostly spherical in shape with the average particle size of 40 μm . The chemical composition of CP-Ti (Ref 16) is shown in Table 1.

An in-house built SLM machine by Advratech LLC (www.advratech.com) (formerly Mound Laser & Photonics Center Inc.) was utilized for single bead experiments. This SLM setup is equipped with Ytterbium fiber laser, which produces a laser beam with a wavelength of 1064 nm and a maximum power of 500 W. A focused laser beam is guided through an optical system to the desired positions of the powder bed to melt the metallic powder. Powder bed is not preheated, and the room temperature was maintained inside the chamber. The argon gas atmosphere was created throughout the chamber. For the current study, single scans were performed for multiple combinations of laser power and scan speed. Also, the laser beam diameter and layer thickness were maintained constant for all samples.

The experiments were done for two cases: *powder case* and *no-powder case*. For powder case, a 50- μm -thick layer of CP-Ti powder was deposited on CP-Ti substrate. Single beads/welds were produced by melting the layer of powder deposited on the substrate. For *no-powder case*, the laser beam was defocused and was directly scanned on the substrate without using any powder. Defocused beam was used only for *no-powder case* to get wider melt pools as part of a separate study. By taking the laser out of focus but increasing the power can affect more material, so the interaction creates a greater melt pool width. In

addition, defocusing of the laser lowers the peak laser intensity, thereby avoiding the attainment of localized extreme temperature. The two samples were prepared: (a) *powder case* CP-Ti samples with 25 beads and (b) *no-powder case* CP-Ti samples with 9 beads. Process parameters used to create the samples are presented in Tables 2 and 3. Images of the created samples

viewed from the top are shown in Fig. 1 and 2 for *powder case* and *no-powder case*, respectively.

3. Results and Discussion

3.1 Surface Morphology of Single Beads

3.1.1 Powder Case. For *powder case*, a thin layer of metal powder was spread on a CP-Ti substrate plate. The single beads were generated by melting deposited powder on the substrate plate by forming uniform melt pool and solidified together (Fig. 3). The variation in the width of a single bead along the track was not significant, except at the start and end points of melted region. The melt pool is wider and rounded at these areas as shown in Fig. 3 due to scanning speed fluctuation while shifting from one bead to other. All the created single beads were continuous and consistent as shown in Fig. 4, and no balling phenomena was observed in the experimented laser power and scan speed range. In the perspective of balling effect and consistency in the melt pool, the selected laser powers and scan speeds are in optimum range.

3.1.2 No-Powder Case or Substrate Remelting. For *no-powder case*, laser scans were performed on a bare substrate plate and single beads were formed by remelting and solidification of the substrate material. The surface roughness of melt pools is much better in *no-powder case*, as seen in Fig. 5 because of the fact that the melt pool is confined within the substrate with no apparent sideways movement. The bead width increases in the scan direction (left to right) due to the heating up of the substrate during the melting process. The higher temperature gradient results in higher melt pool temperature that causes the melt pool to be wider in the scan direction (Ref 17). Also due to speed fluctuations in laser, while shifting to next spot, the melt pool is narrow and rounded at the start and no melt pool formation at the end. Bead formation are not consistent (narrow width or discontinuity observed) at higher scan speeds. Inconsistency in bead formation is shown in Fig. 6 where laser power is 276 W and laser scan speed is 100 mm/s. Niu and Chang (Ref 18) also found instability of scan tracks of sintered high-speed steel powder at higher scan speeds though the process parameter sets were different. For *no-powder case*, balling phenomena was not observed.

3.2 Melt Pool Geometry

After melting single beads on the substrate, the melt pool geometries such as melt pool width, depth, and height for each single bead were measured using an optical microscope.

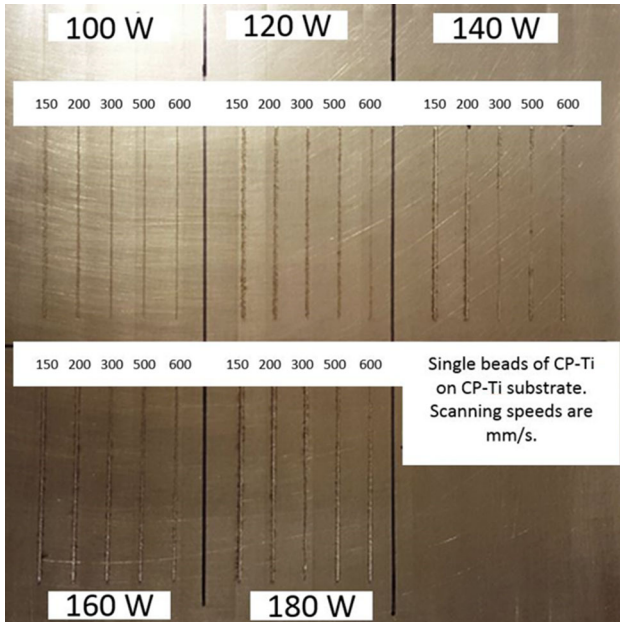


Fig. 1 CP-Ti sample (*powder case*) with 25 beads

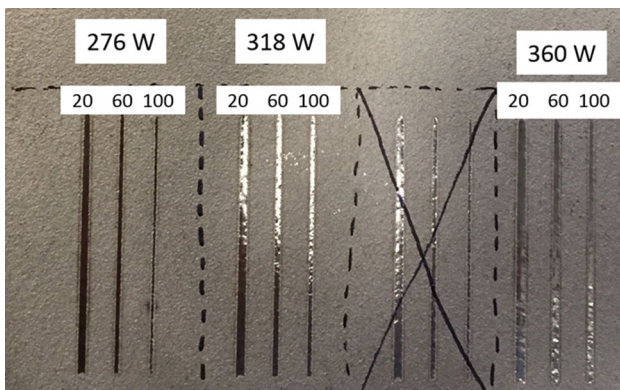


Fig. 2 CP-Ti sample (*no-powder case*) with 9 beads

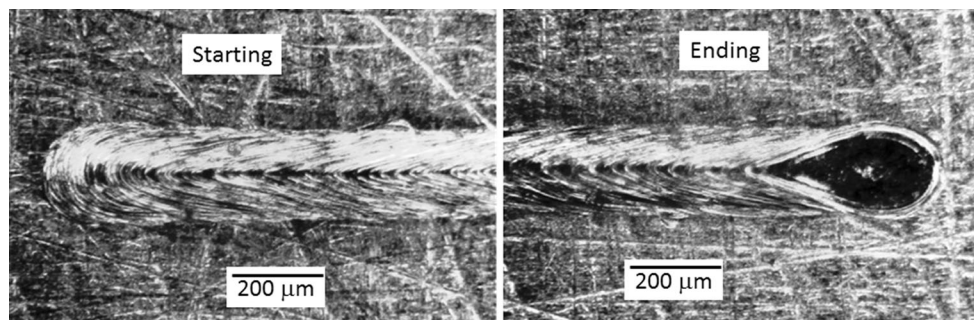


Fig. 3 Start and end points of *powder case* CP-Ti single beads (140 W and 500 mm/s)

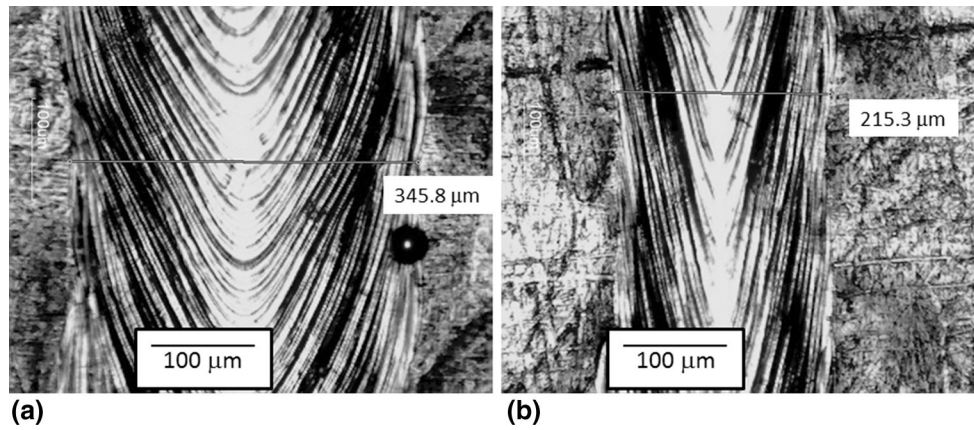


Fig. 4 Consistent melt pool of *powder case* CP-Ti sample: (a) 180 W and 200 mm/s and (b) 180 W and 500 mm/s. The figure also shows the measurement of melt pool width

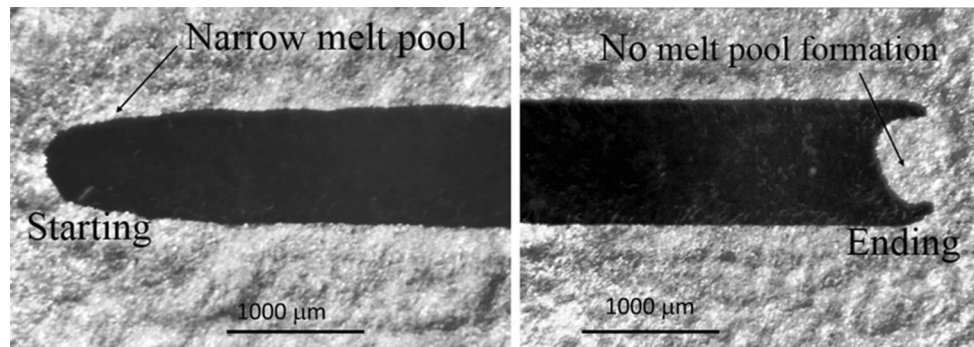


Fig. 5 Start and end points of *no-powder case* single beads (318 W and 20 mm/s)

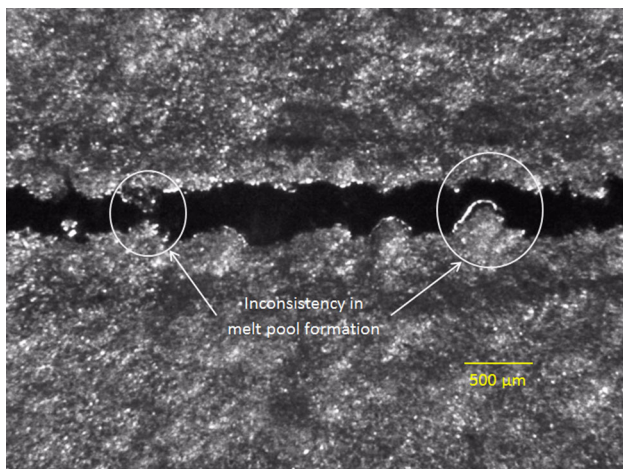


Fig. 6 Inconsistency or non-uniformity in melt pool width at 276 W and 100 mm/s

Figure 7 shows a schematic diagram of the melt pool profile and geometry.

3.2.1 Melt Pool Width. The width of each single bead was measured using optical microscopy (OM) at multiple locations away from the starting and ending points for all single beads. Representative OM images are shown in Fig. 4 and 8 for *powder case* and *no-powder case*, respectively. Multiple

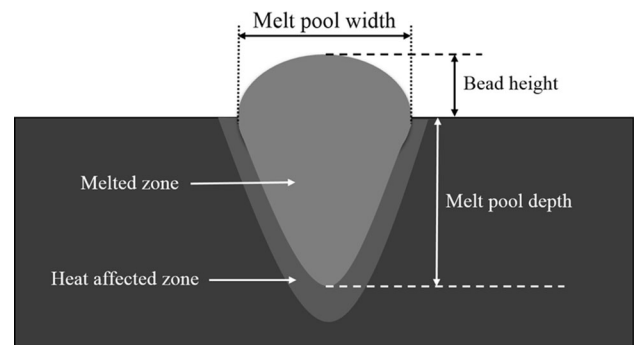


Fig. 7 Schematic diagram showing melt pool profile and geometry

measurements of the solidified melt pool ensure an acceptable trend of the average melt pool width with laser power and scan speed. The average melt pool width measurements at different laser power P and scan speed v are summarized in Table 4 for *powder case* and in Table 5 for the *no-powder case*. It can be concluded from the very low percentage standard deviation that the created beads were mostly uniform except for the *no-powder case* samples created at higher scan speeds (100 mm/s). Relatively high standard deviation in this case further confirms the non-uniformity in melt pool formation. By combining these two laser parameters into one single parameter, LED (J/mm) was calculated using Eq 1 for

different P and v , where P is in J/s and v is in mm/s. The effect of LED on melt pool width is shown in Fig. 9. A similar step was followed for the *no-powder case* where the effect of LED on melt pool width is shown in Fig. 10.

From the presented results, it is clear that the high power and slow scan speed lead to wider melt pools, whereas low power combined with higher scan speed results in narrow melt pools. It is clear from Table 4 (*powder case*) and Table 5 (*no-powder case*) that the width of solidified melt pool increases with laser power and decreases with scan speed keeping all other parameters constant. Figure 9 (*powder case*) and Fig. 10 (*no-powder case*) show that higher laser energy density causes wider melt pool and vice versa. These results are consistent with Ti-64 material reported in Ref 19. The variation of melt pool width as a function of energy density can be represented with a curve fit, which gives the melt pool width value at a

particular LED. As shown in Fig. 9, the melt pool width and linear energy density E can be related using the following equation for *powder case*:

$$\text{Melt pool width, } w = 104.91 \ln(E) + 325.46 \quad (\text{Eq 2})$$

Equation 2 can also be written in terms of laser power P and scan speed v as

$$\text{Melt pool width, } w = 104.91 \ln(P/v) + 325.46 \quad (\text{Eq 3})$$

Similarly, for the *no-powder case*, the melt pool width and linear energy density E can be related using the following equation as shown in Fig. 10:

$$\text{Melt pool width, } w = 327.85 \ln(E) + 45.16 \quad (\text{Eq 4})$$

Equation 4 can be also written in terms of laser power P and scan speed v as

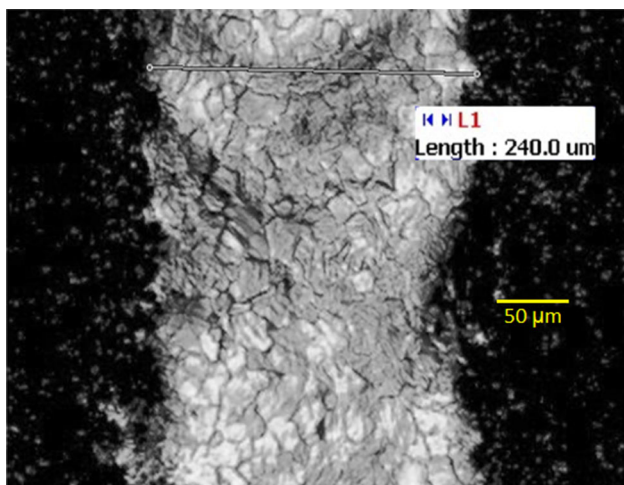


Fig. 8 Measuring melt pool width, *no-powder case*, 276 W and 100 mm/s

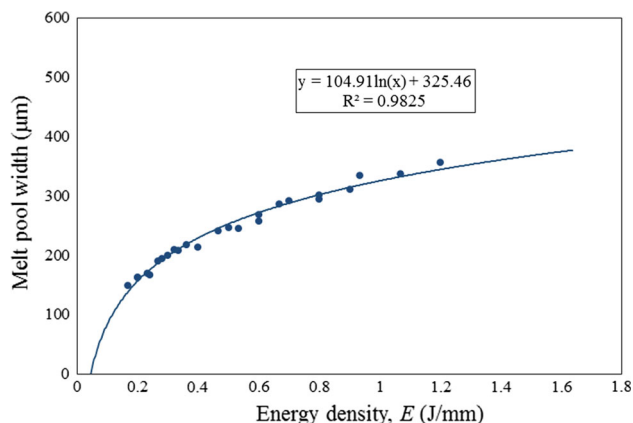


Fig. 9 Effect of energy density on melt pool width for *powder case* samples

Table 4 Average melt pool width measurements with standard deviation (SD) of *powder case* samples in μm

Laser power, P , W	Scan speed, v , mm/s									
	150		200		300		500		600	
	Mean	SD, %	Mean	SD, %	Mean	SD, %	Mean	SD, %	Mean	SD, %
100	286.5	0.8	247.2	1.5	208	0.7	163	2.1	149.2	3.1
120	301.2	1.5	258.2	1.0	214.2	3.4	167.7	3.0	163.7	0.2
140	335	7.7	292.7	1.9	241.5	0.7	194.7	3.5	170	3.0
160	337.5	0.6	295.5	0.7	245	2.8	210.2	1.7	190.3	1.3
180	356.7	6.5	311.7	8.3	268.5	3.0	217.5	1.0	200	3.6

Table 5 Average melt pool width measurement with standard deviation (SD) of *no-powder case* samples in μm

Laser power, P , W	Scan speed, v , mm/s					
	20		60		100	
	Mean	SD, %	Mean	SD, %	Mean	SD, %
276	829.5	9	461.1	3.6	294.2	10.4
318	953.9	5.7	629.9	7.8	430.5	16.9
360	1018.5	5.6	715.9	5.6	554.2	5.3

$$\text{Melt pool width, } w = 327.85 \ln(P/v) + 45.16 \quad (\text{Eq 5})$$

Units for different variables used in Eq 2 through 5 are as follows: w is in mm, E is in J/mm, P in W, and v is in mm/s. The above equations can be used to estimate melt pool width at a particular laser power and scan speed for additive manufacturing process (*powder case*) or laser surface modification (*no-powder case*) processes.

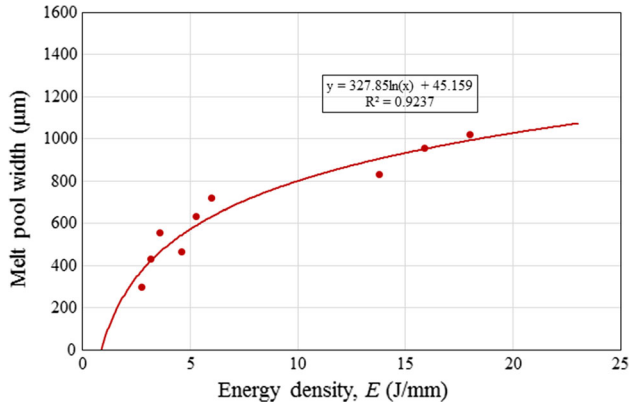


Fig. 10 Effect of energy density on melt pool width for *no-powder case* samples

It is clear from Eq 2 and 4 that there exists a threshold linear energy input rate (E_{th}) below which no melting occurs (or $w = 0$). The threshold linear energy input rate values are 0.045 J/mm for *powder case* and 0.87 J/mm for the *no-powder case*. It may be noted here that laser beam diameters for *powder case* and *no-powder case* are 100 and 115 μm , respectively. It is thus concluded that for almost similar beam diameter, a higher energy density is needed for the *no-powder case* as compared to *powder case*. While comparing different publications, it is observed that the surface remelting of bulk titanium (Ref 6, 7) has been done at higher LED (Ref 6) as compared to titanium powder (Ref 13-15). For example, LED used for surface remelting of bulk titanium is found to be 55-200 J/mm in Ref 6 and 13-113 J/mm in Ref 7. In contrast, lower LED values are used for SLM of CP-Ti powder, for example 0.2-10 J/mm in Ref 13, 20. Threshold LED is the minimum LED needed for the melt pool temperature to exceed its melting point. Peak melt pool temperature depends upon the nature of laser/material interaction (Ref 14) as well as its thermal properties such as diffusivity (Ref 14, 21). When a laser beam interacts with a smooth metallic surface, the beam energy is first absorbed in a narrow layer determined by the optical penetration depth of the radiation into the bulk material. For most bulk metallic materials, the optical penetration depth is in the range of several nanometers. On the other hand, the optical properties of metallic powders with particle sizes in the range of the optical wavelength and above are different from those of bulk materials. Because of its morphology such as surface

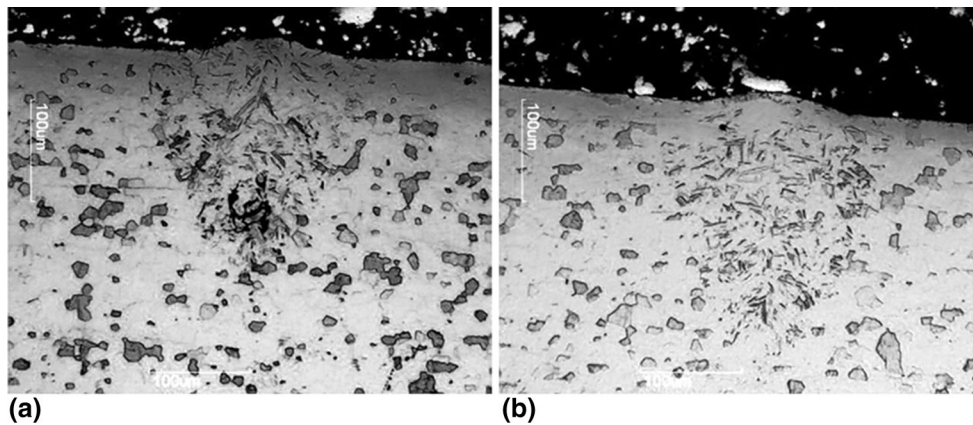


Fig. 11 Melt pool profiles of *powder case* sample: (a) 120 W and 100 mm/s and (b) 140 W and 100 mm/s

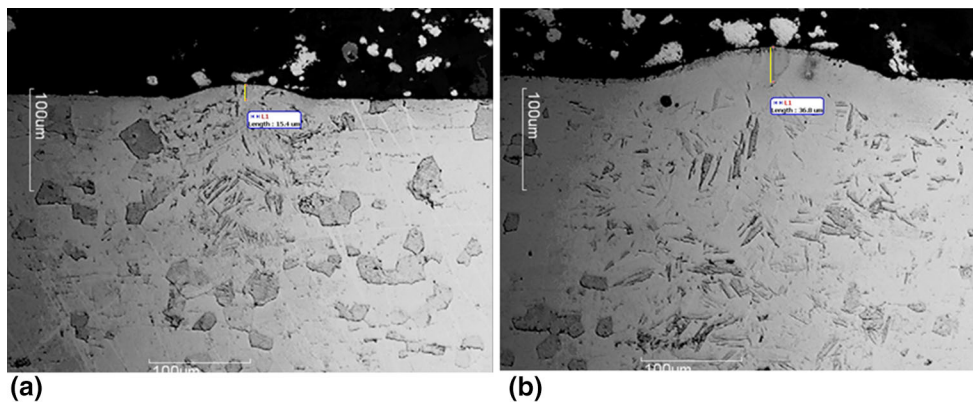


Fig. 12 Measuring bead height for *powder case* samples: (a) for 160 W and 600 mm/s samples and (b) for 160 W and 150 mm/s

Table 6 Bead height measurement of CP-Ti powder case samples in μm

Laser power, P , W	Scan speed, v , mm/s				
	150	200	300	500	600
100	22.4	13.4	11.9	7.5	7
120	27.9	23.9	21.4	13.9	10.4
140	27.4	23.4	22.2	15.9	11.9
160	36.8	29.4	22.9	20.9	15.4
180	37.3	34.3	27.9	21.4	15

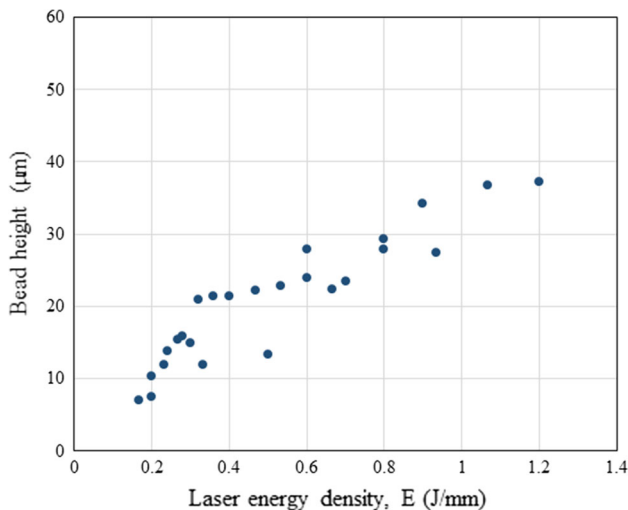


Fig. 13 Effect of laser energy density on bead height for powder case samples

roughness and voids between particles, optical penetration depths are larger than in bulks and are in the order of microns due to multiple reflections within the powder layer (Ref 14). Further energy input causes heat flow within the material. It is mentioned here that thermal diffusivity for bulk material is higher than powder material. Higher the thermal diffusivity, lower is the peak melt pool temperature. Thus, higher LED is needed for bulk material to cause melting as evidenced in Ref 21.

3.2.2 Melt Pool Profiles. All single beads were sectioned in the middle (far away from the start and end points), perpendicular to the scanning direction, using electronic discharge machine (EDM). The sectioned samples were mounted in 50 mm diameter mounts, and the cross sections were polished and etched using standard metallographic preparation methods. For all the samples, the melt pool profiles were not clearly visible because both materials in the melt pool and the substrate are the same (CP-Ti). However, the heat-affected zone is shown in Fig. 11. The melt pool depths were not measured in this study.

3.2.3 Bead Height. The height of each single bead was measured using an optical microscope (OM) according to the measuring scheme shown in Fig. 7 for powder case only because the surface remelting of no-powder case samples did not have any differentiable height relative to the substrate as no

Table 7 Hardness ratio measurements of powder case samples

Laser power, P , W	Scan speed, v , mm/s				
	150	200	300	500	600
100	0.979	0.993	0.903	0.958	0.972
120	0.903	0.958	0.910	0.958	1.006
140	1.006	1.000	0.875	0.862	0.862
160	0.896	0.931	0.903	0.979	0.937
180	0.882	1.000	0.924	0.882	0.813

material was added. A similar technique is used by Hong et al. (Ref 22) to find bead height of sintered Co-Cr alloy. Representative OM images of bead height measurement is shown in Fig. 12(a) for 160 W and 600 mm/s samples and Fig. 12(b) for 160 W and 150 mm/s samples where bead height is indicated by a line. Figure 12 shows that bead height as well as melt pool volume are higher at higher LED (or at a lower scan speed for constant power). Powder and base plate appear to be melted and fused together to form a melt pool. For the process window, all the powder case samples have significantly deeper melt pools than the powder layer thickness. This means that, besides melting powder, most of the radiation energy is converted to thermal energy to form a melt pool and then conducted downwards to the base plate. The measured bead height for different laser power P and scan speed v is summarized in Table 6. From this table, an increasing trend in bead height with laser power and decreasing trend with scan speed is observed. Laser power is divided by scan speed to calculate LED according to Eq 1, and bead height is plotted against LED that is shown in Fig. 13. It is observed that the bead height increases with the increase in laser energy density and vice versa. The data shown in Fig. 13 are little scattered as only one measurement was considered for each process condition; however, the increasing trend is clear from the plot. Lower the LED, lower is the volume exceeding melting point and the amount of powder to be melt, and vice versa. Thus, the bead height is expected to increase with increasing LED although the layer thickness was same for all cases. This result is consistent with data presented in references (Ref 19, 22). Hong et al. (Ref 22) suggested that other probable reason for this phenomenon could well be the Marangoni convection in the melt pool.

3.3 Hardness of Solidified Beads

The hardness of solidified melt pool was measured using micro-Vickers hardness tester, operating at indent force of 500 g and indentation time of 13 s. The indentations were applied on the polished surface of melt pool regions for powder case samples. Only one measurement was taken for each melt pool as the area of sectioned melt pool was small, which did not allow for multiple indentations. Since the bead surfaces of no-powder case samples were relatively smooth as shown in Fig. 5 and 6, the solidified melt pool surface was indented at multiple points along the bead length to get average hardness. The ratio of bead hardness to substrate hardness is termed “hardness ratio” in this study and is plotted for different LED. The substrate hardness was measured away from the laser created beads.

Table 8 Hardness ratio measurements of *no-powder case* samples

Laser power, P , W	Scan speed, v , mm/s					
	20		60		100	
	Mean	SD, %	Mean	SD, %	Mean	SD, %
276	0.984	0.9	1.006	0	0.970	3.6
318	0.939	2.9	1.006	0	0.977	3.4
360	0.846	0.3	1.006	0	1	6.4

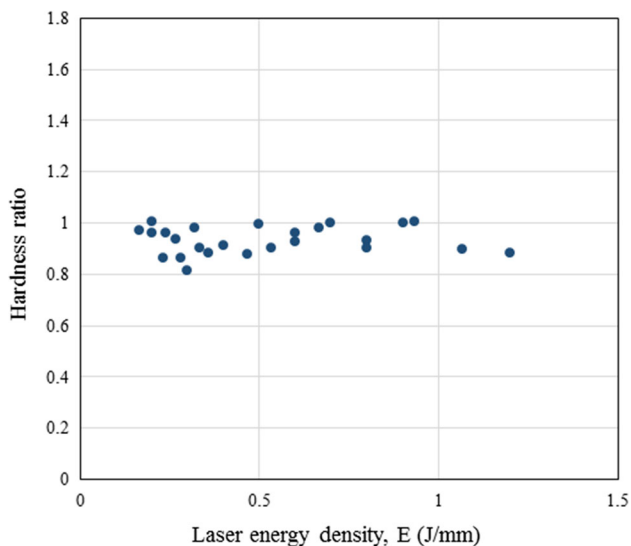


Fig. 14 Hardness ratios at each energy density E for *powder case* samples

The measured hardness data for *powder case* and *no-powder case* samples are summarized in Tables 7 and 8, respectively. It is hard to identify the individual effect of laser power and scan speed on the hardness of solidified melt pools from the tabulated data. To have a better understanding, LED was calculated from Tables 7 and 8 and hardness ratio is plotted against LED in Fig. 14 and 15 for *powder case* and *no-powder case*, respectively. Figure 14 shows that there is no clear trend of hardness variation for *powder case* within the LED range of 0.2–1.2 J/mm. For *no-powder case* samples, the solidified melt pool hardness appears to go down beyond the laser energy density of approximately 10 J/mm. Upon cooling from the molten liquid, CP-Ti first solidifies as the body-centered cubic β -phase which subsequently transforms to the hexagonal close-packed α -phase upon crossing the transformation temperature of 882 °C. Under slow cooling, this transformation is a diffusional process resulting in an equiaxed α microstructure. Rapid cooling results in the formation of the α' phase through a diffusionless (martensitic) transformation, especially in the presence of impurities, such as Fe which is often found in CP-Ti. However, the martensitic transformation has little effect on the strength and hardness of the alloy. It is therefore not surprising that very little variation in hardness is observed for over the entire range of LEDs used for the *powder cases* in this study (Fig. 14). For the *no-powder* (surface remelting) case, there is a trend toward decreased hardness at high LEDs (Fig. 15). The high energy input would result in the metal being heated to a higher temperature and remaining hot for a longer period of time. Generally, longer times at higher temperatures result in an increase in grain size and a correspond-

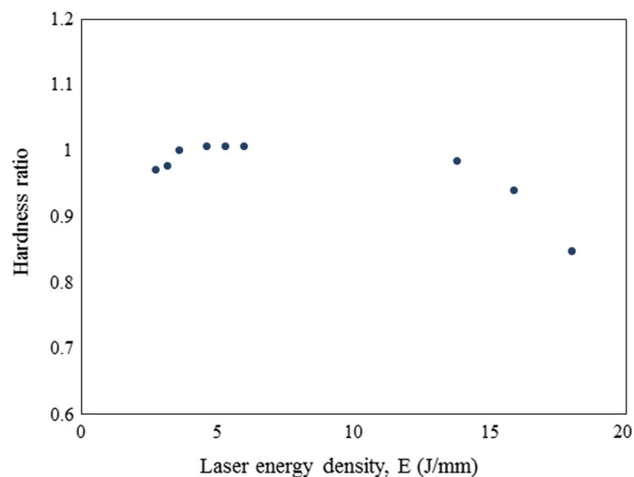


Fig. 15 Hardness ratios at each energy density E for *no-powder case* samples

ing decrease in the strength and hardness of CP-Ti (Ref 23). A publication detailing the effect of LED on the microstructure of CP-Ti for the experimental conditions presented in this article is under preparation. A similar observation of relatively constant hardness at lower LED and decreased hardness at higher LED has been reported in Ref 13, 20 for CP-Ti. They observed the microhardness in SLM built CP-Ti samples to be relatively constant when using LED in the range of 1.0 and 2.5 J/mm, but decreasing hardness was observed at higher LEDs.

4. Summary

In this study, single tracks of CP-Ti were produced by an in-house built-in SLM machine under argon gas shielding atmosphere without preheating the bed at room temperature and pressure. CP-Ti is used as both substrate and powder material. Two types of samples were prepared: one sample by melting a powder layer on the substrate and another sample by remelting the bare substrate. A combination of laser power and laser scan speed was used for single bead fabrication, while the laser beam diameter (100 μm for *powder case* and 115 μm for the *no-powder case*) as well as the powder layer thickness of 50 μm was kept constant.

The solidified melt pools were subjected to physical and mechanical tests. It is observed that melt pool width increases semilogarithmically with laser energy density. There appears to be a threshold energy density below which no melting occurs. The threshold energy density for the *powder case* samples is

much lower than that for the *non-powder case* samples. Bead height of the *powder case* samples appears to increase with energy density although all the samples were created with the same powder layer thickness. For this case, no variation in hardness is observed as the energy density is very low. However, hardness for the *no-powder case* appears to decrease when the energy density is very high.

Acknowledgments

The authors acknowledge the financial support from Advratech (Grant. # 669845) (NASA Prime, Grant # NNX15CM65P). The authors thank the Advratech engineers for creating the single bead samples for the study.

References

1. A. Stwora and G. Skrabalak, Influence of Selected Parameters of Selective Laser Sintering Process on Properties of Sintered Materials, *J. Achiev. Mater. Manuf. Eng.*, 2013, **61**(2), p 375–380
2. C.Y. Yap, C.K. Chua, Z.L. Dong, Z.H. Liu, D.Q. Zhang, L.E. Loh, and S.L. Sing, Review of Selective Laser Melting: Materials and Applications, *Appl. Phys. Rev.*, 2015, **2**, p 041101
3. N.T. Aboukhaireh, N.M. Everitt, I. Ashcroft, and C. Tuck, Reducing Porosity in AlSi10Mg Parts Processed by Selective Laser Melting, *Addit. Manuf.*, 2014, **1-4**, p 77–86
4. T. Kurzynowski, E. Chlebus, B. Kuźnicka, and J. Reiner, Parameters in selective laser melting for processing metallic powders, *Proceedings of SPIE 8239, High Power Laser Materials Processing: Lasers, Beam Delivery, Diagnostics, and Applications*, San Francisco, California, USA, 2012
5. G. Cotogno, U. Holzwarth, M. Franchi, S. Rivetti, and R. Chiesa, Tribological Characterization of Surface-Treated Commercially Pure Titanium for Femoral Heads in Total Hip Replacement: A Feasibility Study, *Int. J. Artif. Organs*, 2006, **29**(12), p 1174–1184
6. A. Lisiecki and A. Klimpel, Diode Laser Surface Modification of Ti6Al4V Alloy to Improve Erosion Wear Resistance, *Arch. Mater. Sci. Eng.*, 2008, **32**(1), p 5–12
7. Z. Sun, I. Annergren, D. Pan, and T.A. Mai, Effect of Laser Surface Remelting on the Corrosion Behavior of Commercially Pure Titanium Sheet, *Mater. Sci. Eng., A*, 2003, **345**(1-2), p 293–300
8. B. Zhang, H. Liao, and C. Coddet, Effects of Processing Parameters on Properties of Selective Laser Melting Mg-9%Al Powder Mixture, *Mater. Des.*, 2012, **34**, p 753–758
9. A. Barbas, A.-S. Bonnet, P. Lipinski, R. Pesci, and G. Dubois, Development and Mechanical Characterization of Porous Titanium Bone Substitutes, *J. Mech. Behav. Biomed. Mater.*, 2012, **9**, p 34–44
10. P. Lipinski, A. Barbas, and A. Bonnet, Fatigue Behavior of Thin-Walled grade 2 Titanium Samples Processed by Selective Laser Melting. Application to Life Prediction of Porous Titanium Implants, *J. Mech. Behav. Biomed. Mater.*, 2013, **28**, p 274–290
11. H. Attar, M. Calin, L. Zhang, S. Scudino, and J. Eckert, Manufacture by Selective Laser Melting and Mechanical Behavior of Commercially Pure Titanium, *Mater. Sci. Eng., A*, 2014, **593**, p 170–177
12. I. Tolosa, F. Garciandía, F. Zubiri, F. Zapirain, and A. Esnaola, Study of Mechanical Properties of AISI, 316 Stainless Steel Processed by “Selective Laser Melting”, Following Different Manufacturing Strategies, *Int. J. Adv. Manuf. Technol.*, 2010, **51**, p 639–647
13. B. Zhang, H. Liao, and C. Coddet, Selective Laser Melting of Commercially Pure Ti Under Vacuum, *Vacuum*, 2013, **95**, p 25–29
14. P. Fischer, V. Romano, H.P. Weber, N.P. Karapatis, E. Boillat, and R. Glatton, Sintering of Commercially Pure Titanium Powder with a Nd:YAG Laser Source, *Acta Mater.*, 2003, **51**, p 1651–1662
15. D. Gu, Y.-C. Hagedorn, W. Meiners, G. Meng, R.J.S. Batista, K. Wissenbach, and R. Poprawe, Densification Behavior, Microstructure Evolution, and Wear Performance of Selective Laser Melting Processed Commercially Pure Titanium, *Acta Mater.*, 2012, **60**(9), p 3849–3860
16. Cp-Ti—Commercially Pure Titanium Powder - AP&C. (n.d.). Retrieved May 20, 2016, from <http://advancedpowders.com/our-plasma-atomized-powders/products/cp-ti-commercially-pure-titanium-powder/>
17. M. Hailat, A. Mian, Z. Chaudhury, G. Newaz, R. Patwa, and H. Herfurth, Laser Micro-Welding of Aluminum and Copper with and Without Tin Foil Alloy, *Microsyst. Technol.*, 2012, **18**(1), p 103–112
18. H.J. Niu and I.T.H. Chang, Instability of Scan Tracks of Selective Laser Sintering of High Speed Steel Powder, *Scripta Mater.*, 1999, **41**(11), p 1229–1234
19. H. Gong, H. Gu, K. Zeng, J.J.S. Dilip, D. Pal, B. Stucker, D. Christiansen, J. Beuth, and J.J. Lewandowski, Melt pool characterization for selective laser melting of Ti-6Al-4V pre-alloyed powder, *Proceedings of the 25th Annual International Solid Freeform Fabrication Symposium*, 2014
20. B. Zhang, H. Liao, and C. Coddet, Microstructure Evolution and Density Behavior of CP Ti Parts Elaborated by Self-Developed Vacuum Selective Laser Melting System, *Appl. Surf. Sci.*, 2013, **279**, p 310–316
21. C.H. Fu, Y.B. Guo, 3-Dimensional Finite Element Modeling of Selective Laser Melting Ti-6Al-4V Alloy, *Proceedings of the 25th Annual International Solid Freeform Fabrication Symposium*, 2014, <https://sffsymposium.engr.utexas.edu/sites/default/files/2014-089-Fu.pdf>
22. M.-H. Hong, B. Min, and T.-Y. Kwon, The Influence of Process Parameters on the Surface Roughness of a 3D-Printed Co-Cr Dental Alloy Produced Via Selective Laser Melting, *Appl. Sci.*, 2016, **6**(2), p 401
23. G.A. Salishchev and S.Y. Miranov, Effect of Grain Size on the Mechanical Properties of Commercially Pure Titanium, *Russ. Phys. J.*, 2001, **44**(6), p 596–601